Supplementary Information

Surface energy alterations derived grain size regulation countering the capacity deterioration in high-voltage single-crystal Ni-rich cathodes

Fuqiren Guo[a], Yang Hu[a], Lang Qiu[a], Yuandi Jiang [a], Yuting Deng[a], Junbo Zhou[a], Zhuo Zheng[b], Yang Liu[c], Yan Sun[d], Zhenguo Wu[a], Yang Song[*a], Xiaodong Guo[a]

a School of Chemical Engineering, Sichuan University, Chengdu, 610065, China.

b The State Key Laboratory of Polymer Materials Engineering, Polymer Research Institute of Sichuan University, Chengdu, 610065, PR China.

c School of Materials Science and Engineering, Henan Normal University, Xinxiang, Henan 453007 PR China.

d School of Mechanical Engineering, Chengdu University, Chengdu, 610106, China.

* Corresponding authors.
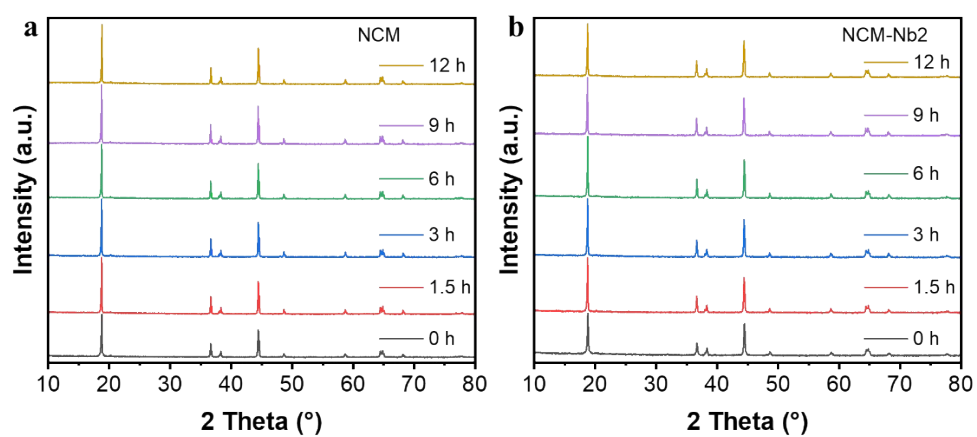
* E-mail addresses: songyang@scu.edu.cn (Yang Song)

Fig. S1 The ex-situ XRD patterns of NCM (a) and NCM-Nb2 (b) collected from 0, 1.5, 3, 9 and 12 h at 840 ℃ under the oxygen atmosphere after quenching.
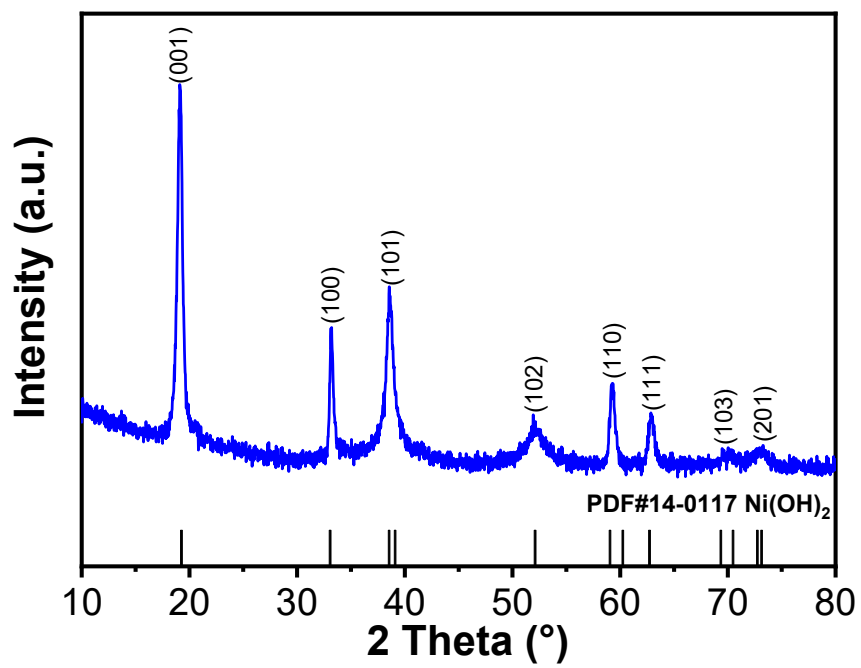
Fig. S2 XRD pattern of precursor synthesized by hydroxide co-precipitation method, which fits well with the $Ni(OH)_2$ phase, and there are no apparent impurity phase.
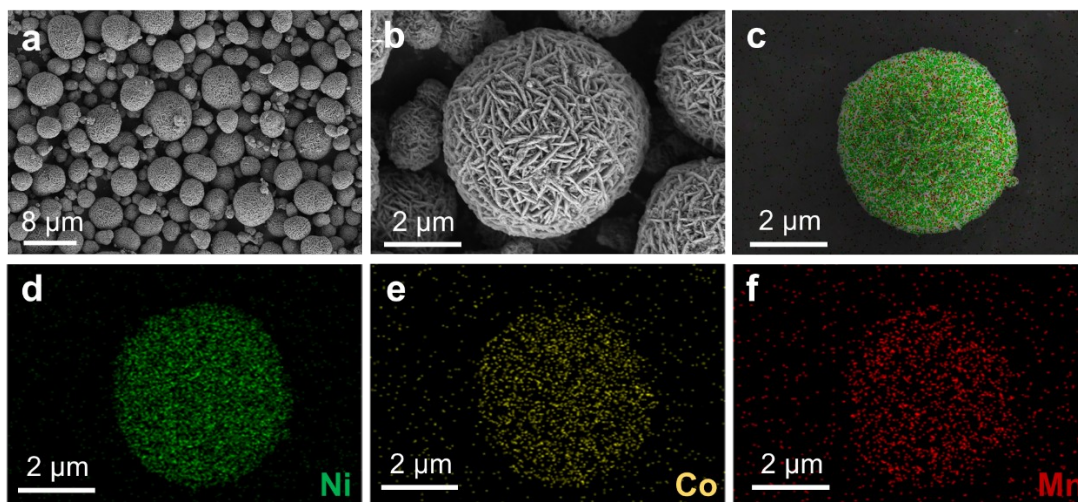
Fig. S3 (a and b) SEM images of precursor. (c-f) The EDS mapping images of precursor, indicating that the Ni, Co and Mn elements uniformly distribute on spherical particles, which is consistent with the original intention of the coprecipitation method, *i.e.*, three elements with different diffusivity are evenly distributed in the entire particle.
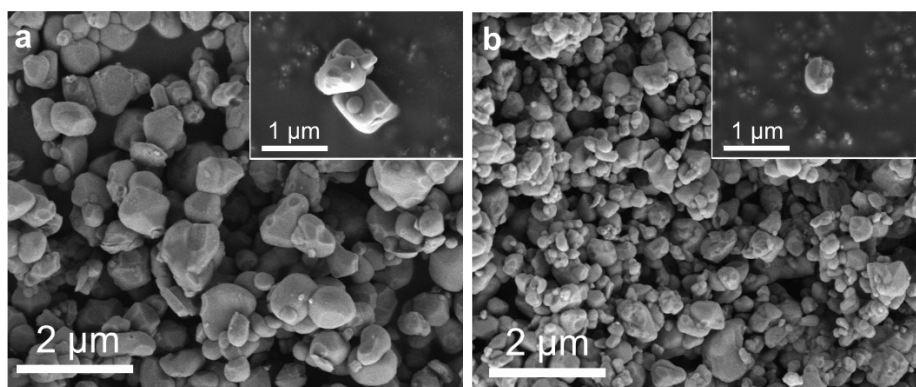
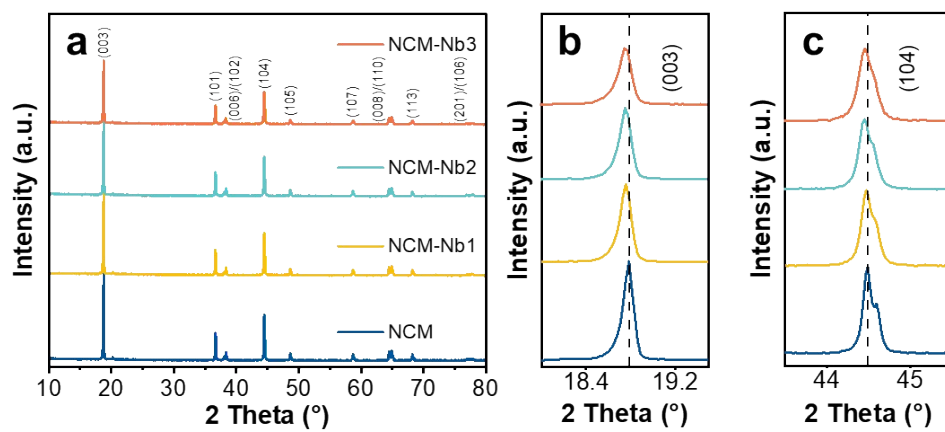**Fig. S4** SEM images of NCM-Nb1 (a) and NCM-Nb3 (b).

Fig. S5 (a) XRD patterns and (b and c) magnified graphs of four samples with or without Nb^{5+} doping.
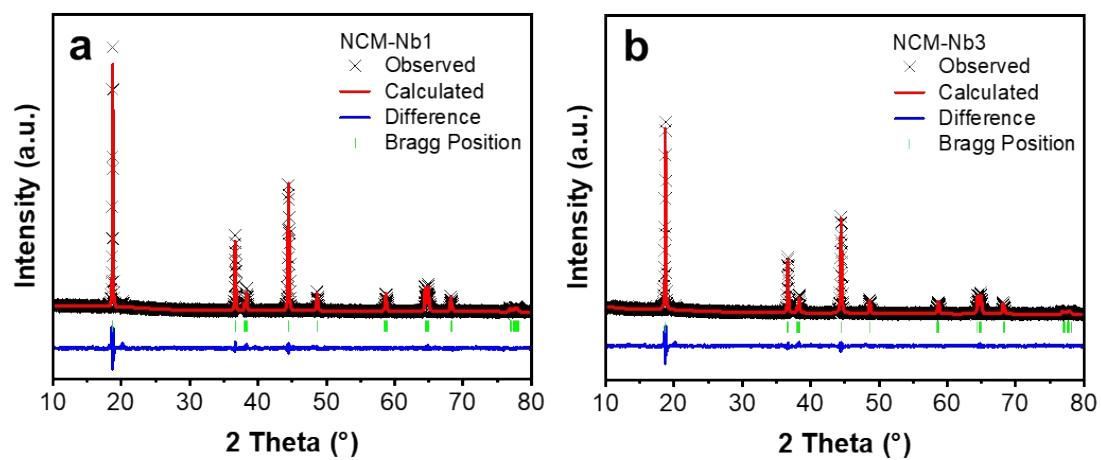
Fig. S6 Corresponding Rietveld refinements of NCM-Nb1 (a), NCM-Nb3 (b).
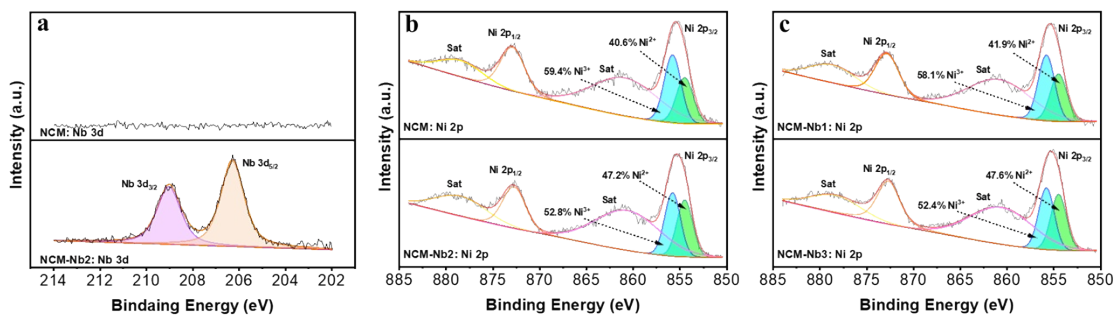
Fig. S7 The corresponding high-resolution XPS spectra of Nb 3d (a), Ni 2p (b and c).
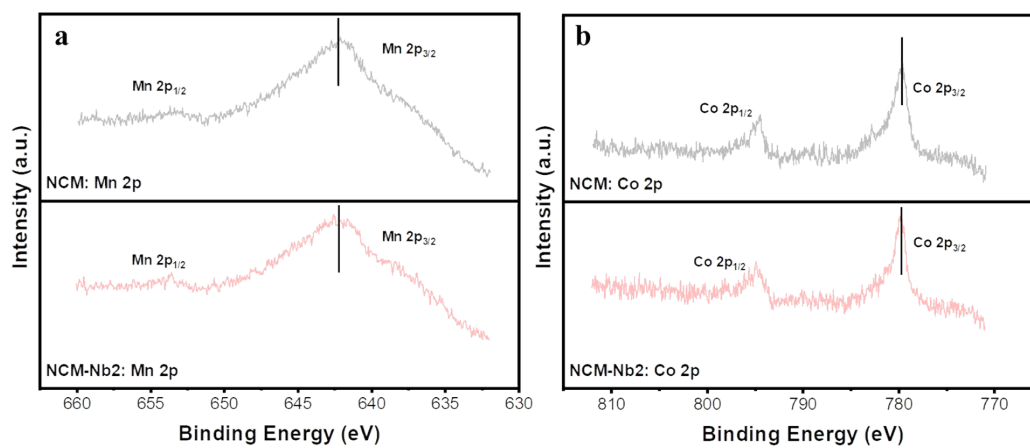
Fig. S8 Surface XPS measurement results of NCM and NCM-Nb2 of (a) Mn 2p. (b) Co 2p.
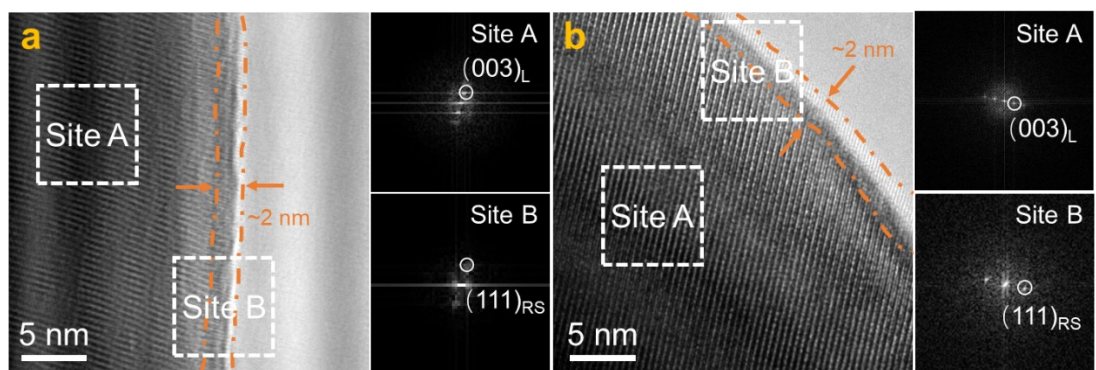
Fig. S9 Two HR-TEM images recorded from different particles for NCM-Nb2. FFT images of selected regions for each particle are shown in the right of a and b. The cation mixing layer on the particle surface of NCM-Nb2 is highlighted by orange dotted line and has a thickness of ~2 nm. It further confirms the existence of the uniform cation mixing layer and the clean surface in different particles.
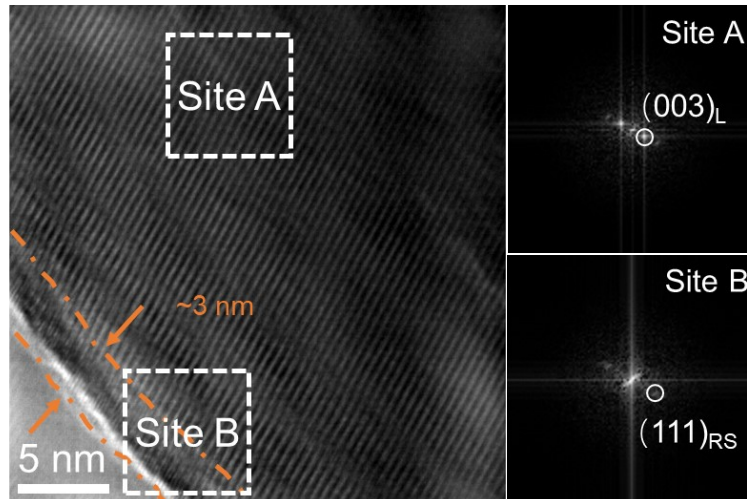
Fig. S10 HR-TEM image of NCM-Nb4 and corresponding FFT images of elected regions. The cation mixing layer on the particle surface of NCM-Nb4 is highlighted by orange dotted line and has a thickness of ~3 nm. The thickness of cation mixing layer is slightly increased compared to NCM-Nb2 (~2 nm). It clearly manifests that increasing the amount of doped Nb^{5+} indeed have a positive effect on the thickness of cation mixing layer.
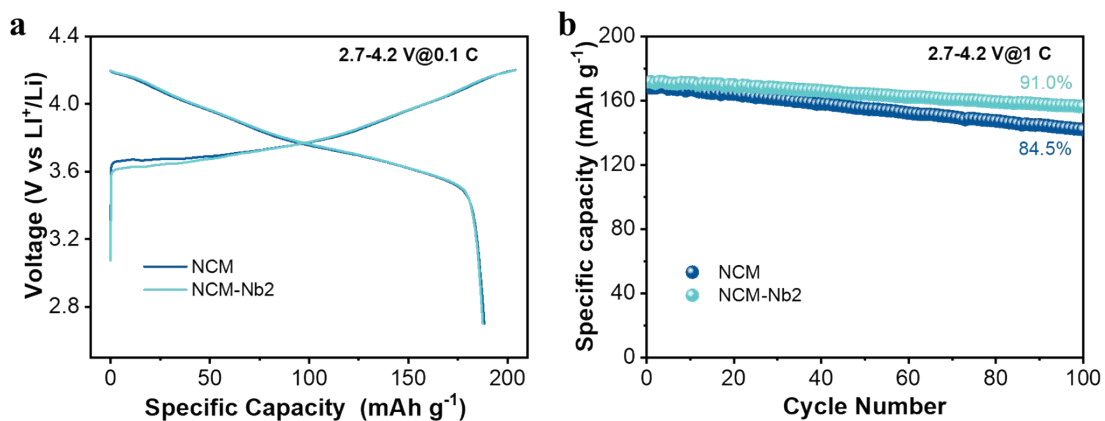
Fig. S11 Electrochemical characterization of half cells for NCM and NCM-Nb2 at 25 °C and between 2.7-4.2 V. (a) The first charge-discharge curves at 0.1 C. NCM and NCM-Nb2 deliver similar capacities of 188.2 and 187.5 mAh g^{-1}, respectively. (b) The cycling curves at 1 C. Obviously, NCM-Nb2 possesses an impressive capacity retention of 91.0% which is higher than that of NCM (84.5%) at a cut-off voltage of 4.2 V.
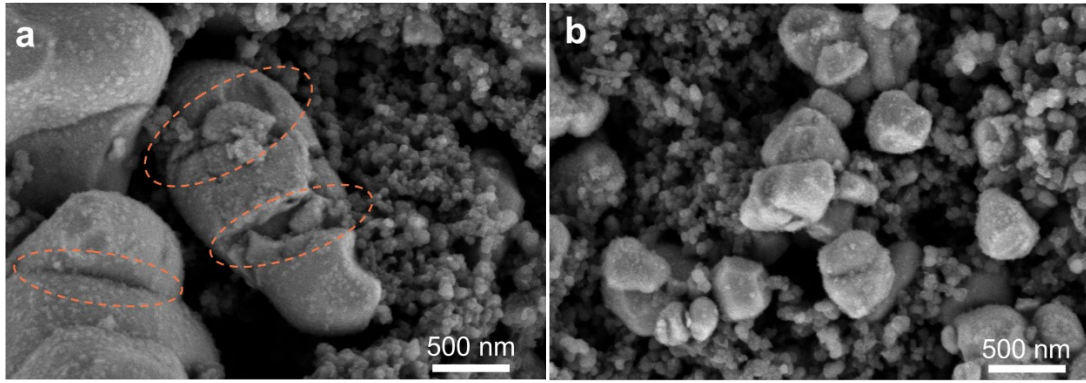
Fig. S12 The SEM images of NCM (a) and NCM-Nb2 (b) after 100 cycles, and the cracks are marked with orange dotted ovals.
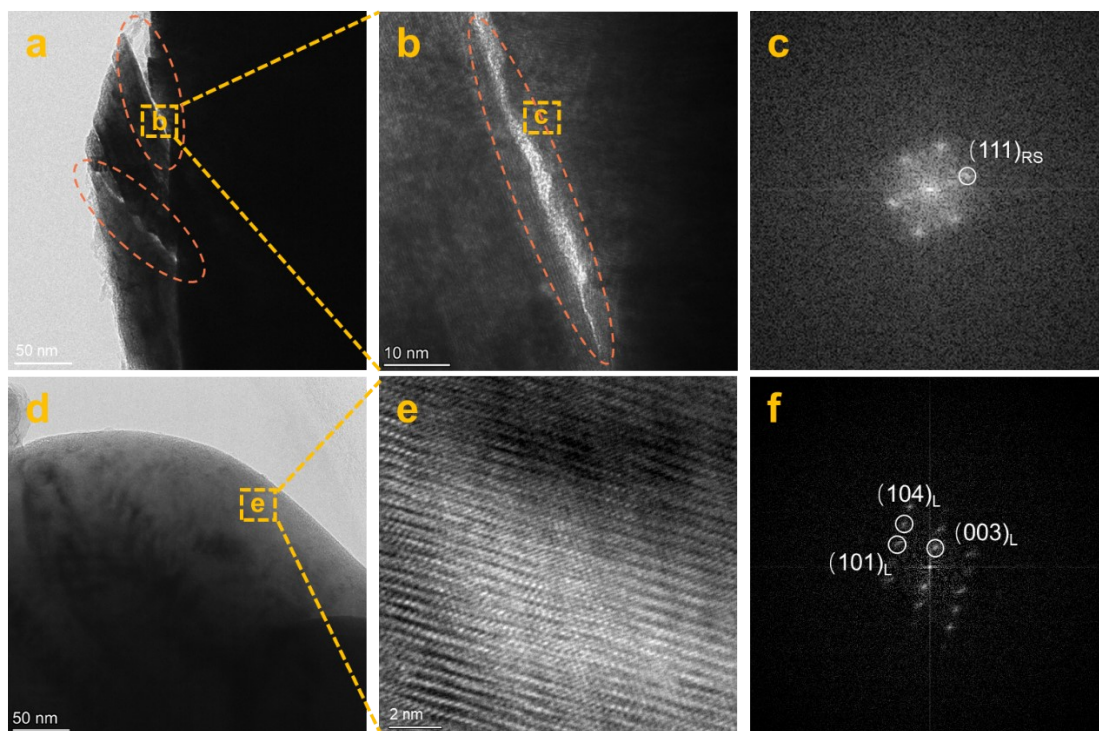
Fig. S13 TEM images along with FFT images of selected regions for NCM (a-c) and NCM-Nb2 (d-f) after 100 cycles, and the intragranular cracks are marked with orange dotted ovals.
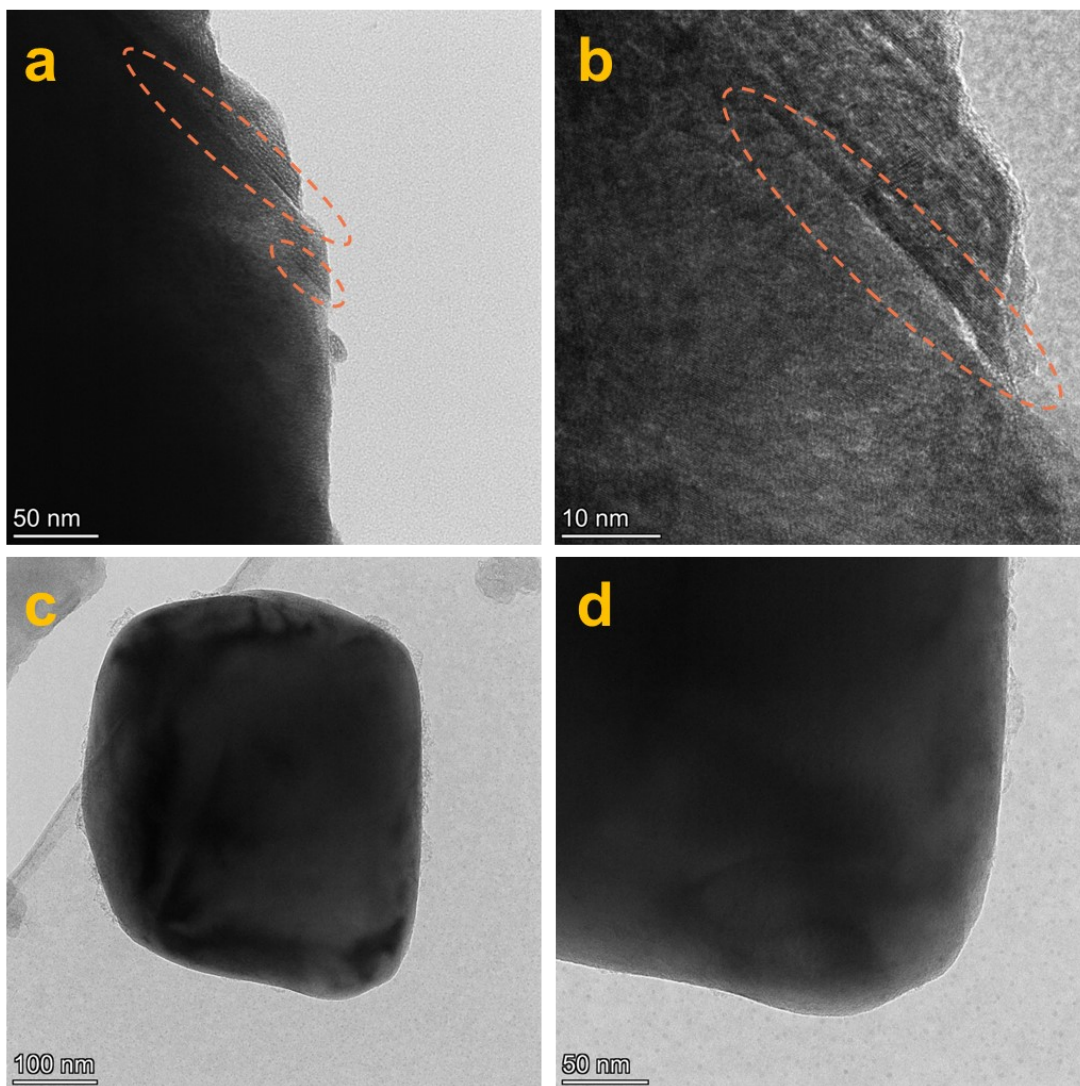
Fig. S14 TEM images for NCM (a-b) and NCM-Nb2 (c-d) which were collected from half-cells after charged to 4.8 V, and the planar slips are marked with orange dotted ovals.
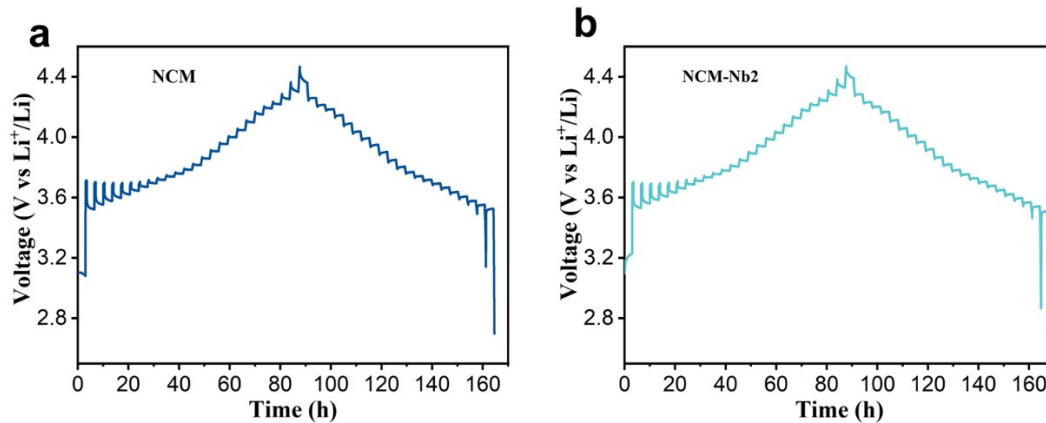
Fig. S15 The GITT curves of NCM (a) and NCM-Nb2 (b) during the 1st charge-discharge process.

Table. S1 Element composition of the precursor by ICP test.

Elements	Ni	Co	Mn
Proportions (mol %)	0.826	0.120	0.054

Table. S2 Surface energy for (001), (012) and (104) faces of pristine and Nb-doped LNO (in J m^{-2}). The reduction is calculated by extracting the energy difference for the Nb-doped and pristine LNO surfaces.

Faces	(001)	(012)	(104)
Pristine	2.274	2.106	0.836
Nb-doped	1.151	1.697	0.715
Reduction	49.4%	19.4%	14.5%

Table. S3 The Rietveld refinement data for NCM, NCM-Nb1, NCM-Nb2 and NCM-Nb3. Importantly, the low values of R_{wp} and R_p infer that it is relatively reliable for these refinement results. Four samples are layered structure with R-3m space group.

Materials	a[Å]	c[Å]	V[Å^3]	Ni^{2+} in Li$^+$ sites	R_p	R_{WP}	$I_{(003)}/I_{(104)}$
NCM	2.8708(0)	14.1844(1)	101.240(2)	0.48%	2.47%	3.71%	2.29
NCM-Nb1	2.8708(0)	14.1891(2)	101.270(2)	1.75%	2.31%	3.29%	2.06
NCM-Nb2	2.8718(0)	14.1944(3)	101.380(4)	2.71%	2.25%	3.17%	2.03
NCM-Nb3	2.8722(0)	14.1973(2)	101.430(3)	3.33%	2.30%	3.23%	1.94

Table. S4 Crystallographic information of NCM (R-3m space group) obtained from Rietveld refinement

Atom	Site	x	y	z	Occ.	Uiso
Li(1)	3b	0.0000	0.0000	0.5000	0.9952	0.0016
Ni(1)	3b	0.0000	0.0000	0.5000	0.0048	0.0016
Li(2)	3a	0.0000	0.0000	0.0000	0.0048	0.0097
Ni(2)	3a	0.0000	0.0000	0.0000	0.8252	0.0097
Co	3a	0.0000	0.0000	0.0000	0.0500	0.0097
Mn	3a	0.0000	0.0000	0.0000	0.1200	0.0097

Atom	Site	x	y	z	Occ.	Uiso
O	6c	0.0000	0.0000	0.2590	1.0000	0.0100

Table. S5 Crystallographic information of NCM-Nb1 (R-3m space group) obtained from Rietveld refinement

Atom	Site	x	y	z	Occ.	Uiso
Li(1)	3b	0.0000	0.0000	0.5000	0.9825	0.0105
Ni(1)	3b	0.0000	0.0000	0.5000	0.0175	0.0105
Li(2)	3a	0.0000	0.0000	0.0000	0.0175	0.0107
Ni(2)	3a	0.0000	0.0000	0.0000	0.8152	0.0107
Co	3a	0.0000	0.0000	0.0000	0.0500	0.0107
Mn	3a	0.0000	0.0000	0.0000	0.1200	0.0107
O	6c	0.0000	0.0000	0.2591	1.0000	0.0100

Table. S6 Crystallographic information of NCM-Nb2 (R-3m space group) obtained from Rietveld refinement

Atom	Site	x	y	z	Occ.	Uiso
Li(1)	3b	0.0000	0.0000	0.5000	0.9729	0.0160
Ni(1)	3b	0.0000	0.0000	0.5000	0.0271	0.0160
Li(2)	3a	0.0000	0.0000	0.0000	0.0271	0.0085
Ni(2)	3a	0.0000	0.0000	0.0000	0.8029	0.0085
Co	3a	0.0000	0.0000	0.0000	0.0500	0.0085
Mn	3a	0.0000	0.0000	0.0000	0.1200	0.0085
O	6c	0.0000	0.0000	0.2607	1.0000	0.0100

Table. S7 Crystallographic information of NCM-Nb3 (R-3m space group) obtained from Rietveld refinement

Atom	Site	x	y	z	Occ.	Uiso
Li(1)	3b	0.0000	0.0000	0.5000	0.9667	0.0170
Ni(1)	3b	0.0000	0.0000	0.5000	0.0333	0.0170
Li(2)	3a	0.0000	0.0000	0.0000	0.0333	0.0116
Ni(2)	3a	0.0000	0.0000	0.0000	0.7967	0.0116
Co	3a	0.0000	0.0000	0.0000	0.0500	0.0116
Mn	3a	0.0000	0.0000	0.0000	0.1200	0.0116
O	6c	0.0000	0.0000	0.2594	1.0000	0.0100

Table. S8 Summary of electrochemical performance data for relevant literatures

Reference	Cathode material	Modified method	Discharge specific capacity at the 100th cycle (mAh g^{-1}) / cycle retention	Rate capacity (mAh g^{-1}, 5C)
Ref. [1]	SC-LiNi$_{0.8}$Co$_{0.1}$Mn$_{0.1}$O$_2$	PMMA coating	156.2 / ~82.5% (4.5 V)	~172.3
Ref. [2]	SC-LiNi$_{0.8}$Co$_{0.1}$Mn$_{0.1}$O$_2$	Ta doping	~174.4/ ~90.4% (4.3 V, 0.5 C)	157 (4 C)
Ref. [3]	SC-LiNi$_{0.7}$Co$_{0.1}$Mn$_{0.2}$O$_2$	Al doping	~145.3 / ~80% (80 cycles)	——
Ref. [4]	SC-LiNi$_{0.9}$Co$_{0.05}$Mn$_{0.05}$O$_2$	Ce doping	~142.2 / ~80.5% (4.3 V, 0.5 C, 30°C)	——
Ref. [5]	SC-LiNi$_{0.83}$Co$_{0.12}$Mn$_{0.05}$O$_2$	B doping	137.2 / ~74% (0.5 C)	——
Ref. [6]	PC-LiNi$_{0.92}$Co$_{0.05}$Mn$_{0.03}$O$_2$	Ti/B co-doping	150 / 78.3%	160.0
Ref. [7]	SC-LiNi$_{0.6}$Co$_{0.2}$Mn$_{0.2}$O$_2$	Al/Zr co-doping	144.2/ 80.1%	——
Ref. [8]	PC-LiNi$_{0.92}$Co$_{0.04}$Mn$_{0.04}$O$_2$	Si doping	157.2 / 75.2 % （0.3 C）	——
This work	**SC-LiNi$_{0.83}$Co$_{0.12}$Mn$_{0.05}$O$_2$**	**Nb doping**	**155.0 / 80.2%; 156.3 / 91.0% (4.2 V)**	**152.3**

Notes: Unless otherwise stated, the cycle tests are performed at 25 ° C, a rate of 1C and an upper cut-off voltage of 4.4V. PC and SC represent poly-crystal and single-crystal, respectively.

Formula. S1 The analytical cylindrical isotropic diffusion-induced-stress model[9]:

$$\Pi = \int \frac{\sigma^2}{2E}dV = \pi * h * \left[\frac{\alpha * E_0 * (C_R - C_0)}{1 - v}\right]^2 * \int_0^r \xi^2 \frac{1}{E}rdr$$

where Π is the strain energy inside grain, h is the height of the cylindrical grain, α is the concentration expansion coefficient, E_0 is Young's modulus of the nonlithiated particle, E is Young's modulus at a given Li-ion concentration, C_R is the Li-ion concentration at the surface, C_0 is the Li-ion concentration at the center, v is Poisson's ratio, ξ represents the dimensionless stress.

Formula. S2 Since only the upper surface was optimized by one dopant atom in this calculation model, the surface energy calculation formula is defined as follows[10]:

$$\gamma = \frac{\Delta E_{sur}}{A} = \frac{1}{2A}(E_{cleaved} - E_{bulk}) + \frac{1}{A}(E_{relaxed} - E_{cleaved})$$

here $\triangle E_{cleaved}$ is the cleaving energy caused by the formation of two new surfaces on both sides of the vacuum slab which is triggered by the bond breaking between the atoms. $\triangle E_{bulk}$ is the energy of the original host crystal. $\triangle E_{relax}$ is the energy change caused by the relaxation of atoms into a stable position near a newly formed surface. In addition, the cross-sectional area A of the three crystal faces, *i.e.*, (001), (012), and (104), are 62.076, 125.917 and 144.890 Å^2, respectively.

Formula. S3 Classical nucleation theory[11]:

$$\Delta G = \frac{4}{3}\pi r^3 \Delta Gv + 4\pi r^2 \gamma$$

here ΔG is the Gibbs free energy change caused by the nucleation, ΔGv is the Gibbs free energy per unit volume caused by the phase transformation, r is the radius of the nuclei, and γ is the surface energy.

Formula. S4 The Li$^+$ diffusion coefficient (D_{Li^+}) can be obtained by performing GITT experiment[12]:

$$D_{Li^+} = \frac{4}{\pi \tau}\left(\frac{m_B V_m}{M_B S}\right)^2 \left(\frac{\Delta E_s}{\Delta E_\tau}\right)^2 \qquad \left(\tau \ll \frac{L^2}{D_{Li^+}}\right)$$

here τ, ΔE_s and ΔE_τ are relaxation time, voltage change during charge (discharge) process and relaxation process, m_B, V_m, and M_B are the mass, molar volume, and molecular weight of the active material, S is the area of the electrode, and L is the length of Li$^+$ ion diffusion.

Notes and reference

1. Y. Han, S. Heng, Y. Wang, Q. Qu and H. Zheng, *ACS Energy Letters*, 2020, **5**, 2421-2433.
2. Y.-G. Zou, H. Mao, X.-H. Meng, Y.-H. Du, H. Sheng, X. Yu, J.-L. Shi and Y.-G. Guo, *Angewandte Chemie International Edition*, 2021, **60**, 26535-26539.
3. L. Cheng, B. Zhang, S.-L. Su, L. Ming, Y. Zhao and X.-X. Tan, *RSC Advances*, 2021, **11**, 124-128.

4.   H.-H. Ryu, S.-B. Lee and Y.-K. Sun, *Journal of Solid State Electrochemistry*, 2022, **26**, 2097–2105.

5.   Y. Liu, X. Fan, B. Luo, Z. Zhao, J. Shen, Z. Liu, Z. Xiao, B. Zhang, J. Zhang, L. Ming and X. Ou, *Journal of Colloid and Interface Science*, 2021, **604**, 776-784.

6.   C. Zhu, M. Cao, H. Zhang, G. Lv, J. Zhang, Y. Meng, C. Shu, W. Fan, M. Zuo, W. Xiang and X. Guo, *ACS Applied Materials & Interfaces*, 2021, **13**, 48720-48729.

7.   Z. Feng, S. Zhang, R. Rajagopalan, X. Huang, Y. Ren, D. Sun, H. Wang and Y. Tang, *ACS Applied Materials & Interfaces*, 2021, **13**, 43039–43050.

8.   D. H. Kim, J. H. Song, C. H. Jung, D. Eum, B. Kim, S. H. Hong and K. Kang, *Advanced Energy Materials*, 2022, **12**, 2200136.

9.   Y. Bi, J. Tao, Y. Wu, L. Li, Y. Xu, E. Hu, B. Wu, J. Hu, C. Wang, J.-G. Zhang, Y. Qi and J. Xiao, *Science*, 2020, **370**, 1313-1317.

10.   Y. Kim, H. Lee and S. Kang, *Journal of Materials Chemistry*, 2012, **22**, 12874–12881.

11.   X. Li, L. Zhou, H. Wang, D. Meng, G. Qian, Y. Wang, Y. He, Y. Wu, Z. Hong, Z.-F. Ma and L. Li, *Journal of Materials Chemistry A*, 2021, **9**, 19675-19680.

12.   C.-L. Xu, W. Xiang, Z.-G. Wu, Y.-D. Xu, Y.-C. Li, M.-Z. Chen, G. XiaoDong, G.-P. Lv, J. Zhang and B.-H. Zhong, *ACS Applied Materials & Interfaces*, 2018, **10**, 27821-27830.